Springer

KSME

Journal of Mechanical Science and Technology 32 (1) (2018) 199~210
www.springerlink.com/content/1738-494x(Print)/1976-3824(Online)
DOI 10.1007/s12206-017-1221-y

The structures of unsteady cavitation shedding flow around an axisymmetric body with a blunt headform †

Changli Hu[1,*], Xuede Wang[1], Guoyu Wang[2] and Youquan Cao[1]

[1]*Nanjing University of Science and Technology, Nanjing 210094, China*
[2]*Beijing Institute of Technology, Beijing 100081, China*

(Manuscript Received July 6, 2017; Revised September 15, 2017; Accepted September 25, 2017)

Abstract

The objective of this paper is to investigate the cavity shedding dynamics in unsteady cavitating flows around an axisymmetric body with a blunt headform. A high-speed video camera is used to record the cavity evolution process. The numerical simulations are performed based on the homogenous method coupled with a modified PANS (Partially-averaged Navier-Stokes) turbulence model and Zwart cavitation model. The results show that the predicted time-evolution process of cavity agree fairly well with the corresponding experimental data for two different cavitation numbers ($\sigma = 0.7$ and $\sigma = 0.6$). Compared to that of $\sigma = 0.6$, the cavity shedding behavior of $\sigma = 0.7$ presents more fluctuations and instabilities. To elucidate the different shedding structures, the Lagrangian coherent structures (LCS) and particle trajectory methods are also utilized here. It is found that the particle tracers respectively demonstrate the cavity shedding behaviors of conjunction at $\sigma = 0.6$ and rolling up at $\sigma = 0.7$. Moreover, the LCS distributions vary with the time-evolution of vortex structures. The particle trajectories can illustrate the upstream and downstream vortex structures connect together at $\sigma = 0.6$ but separate at $\sigma = 0.7$, which highly consistent with the cavity shedding behaviors.

Keywords: Cavity shedding dynamics; Vortex; Lagrangian particle trajectory; Axisymmetric body

1. Introduction

Cavitation is an abrupt phase change phenomenon that often occurs in various technical applications, such as pumps, turbines, ship propellers as well as high-speed under water vehicles [1, 2]. Wang et al. [3] conducted an experiment on 2D hydrofoil and found that by decreasing the cavitation number, four different regimes can be identified including inception cavitation, sheet cavitation, cloud cavitation and supercavitation. Cloud cavitation phenomenon is often caused by sheet cavitation shedding, and is highly related to the hydrodynamic performance and produces vibration, noise and cavitation erosion due to its unsteady characteristics. Owing to its importance in various technical applications, much effort has been made in the past decades to study the unsteady characteristics of cavitation shedding flow.

In the experimental side, numerous experiments have been carried out to study cavitation shedding characteristic especially on hydrofoils [4-6] and axisymmetric bodies [7-9]. These studies have considerably improved the understanding of cavitation shedding characteristic. Kubota et al. [4] investigated the unsteady sheet cavitation shedding flow around an 2D hydrofoil. The pressure fluctuation resulting from unsteady sheet/cloud cavitation was investigated by Leroux et al. [5]. Huang et al. [6] reported that the development process of the unsteady cavitation led to substantial increase in turbulent velocity fluctuations and significantly modified the wake patterns. There are also many experimental studies on unsteady cavitating flows around axisymmetric bodies. For example, Rouse et al. [7] measured the near-wall pressure distribution on different axisymmetric bodies. Liu et al. [8] investigated the frequency characteristics of unsteady cavitation flows around axisymmetric headforms. Hu et al. [9] observed the three-dimensional unsteady cavitating flows around an axisymmetric body.

Due to various limitations in experimental measurement techniques, many efforts have been made in numerical simulations of sheet/cloud cavitation in recent years. Since several researchers [10, 11] indicate that high eddy viscosity of the original Launder-Spalding version of the $k-\varepsilon$ Reynolds-averaged Navier-Stokes (RANS) model [12] can excessively restrain the cavitation instabilities, several hybrid modeling approaches are applied to improve the traditional RANS models, such as, a Filter-based model (FBM) [11], Partially-averaged Navier-Stokes (PANS) [13], and Large Eddy simu-

*Corresponding author. Tel.: +86 25 84315985, Fax.: +86 25 84315985
E-mail address: ghclq@163.com
† Recommended by Associate Editor Shin Hyung Rhee

lation (LES) [14, 15] method. Ji et al. [14] studied the cavitation structures and the shedding dynamics of the cavitating flow around a NACA66 hydrofoil by LES method. Similarly, Yu et al. [15] studied the characteristics of cloud cavity around axisymmetric projectile by LES method. Yang et al. [16] simulated unsteady cavitation shedding around a NACA66 hydrofoil by RANS model and sidewall effect is found to be the main reason for the generation of U-shaped cavitation. Ji et al. [17] investigated unsteady cavitating turbulent flow around a twisted hydrofoil to illustrate the pressure fluctuations mechanism by PANS method. Chen et al. [18] studied the cavitation collapse regime around submerged vehicles navigating with deceleration based on numerical results using the RNG $k-\varepsilon$ turbulence model. Hu et al. [19] proposed a modified PANS model to simulate unsteady cavitating flows around a hydrofoil.

In order to better analyze the unsteady flow structure, the FTLE (Finite-time Lyapunov exponent) and LCS (Lagrangian coherent structures) methods were developed based on the Lagrangian perspective which was presented in Refs. [20, 21]. Green et al. [22] studied the three-dimensional flows via the LCS method and found that the LCS can present greater visible details without the requirement of velocity derivatives. Tang et al. [23] applied the LCS method to assess the three-dimensional unsteady wind field and showed this approach is inherently frame independent and can achieve physical objectivity in continuum mechanics. Also, Zhao et al. [24] utilized the LCS method to analyze the vortex-cavitation interrelations. These researches showed that the LCS is more effective in capturing the dynamical features of the flow, compared with the traditional Eulerian analysis.

Although some researchers have investigated on the unsteady characteristics of sheet cavitation shedding flow, little attention has been given to the comparison between different kinds of sheet cavitation shedding patterns. The objective of the present paper is to investigate the difference of two kinds of sheet cavitation shedding patterns around an axisymmetric body with a blunt headform by both experimental and computational modeling methods. This paper is organized as follows. Firstly, the experimental setup and the numerical model are introduced and discussed. Secondly, the two kinds of unsteady cavity shedding patterns captured by the high-speed video and computational modeling are investigated. Finally, the FTLE method is utilized to get a better understanding of differences between the two kinds of cavity shedding process.

2. Experimental setup and numerical method

The experiments are carried out in a closed-loop cavitation tunnel as shown in Fig. 1(a). An axial flow pump, which is used to drive the flow in the tunnel, is located about 5 m below the test section to reduce the likelihood of pump cavitation. A tank with a volume of 5 m^3 is placed upstream of the test section to separate the undesired free stream bubbles. The top of the tank is connected to a vacuum pump, which is used

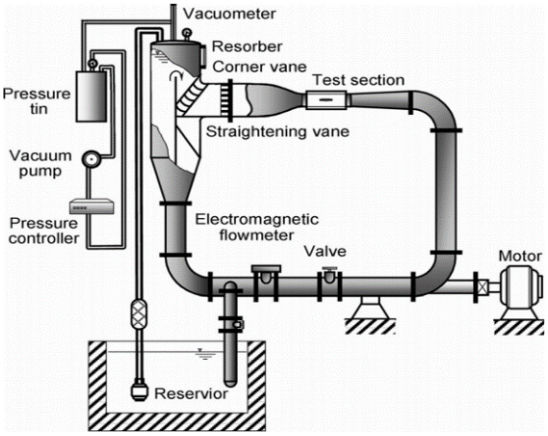

(a)

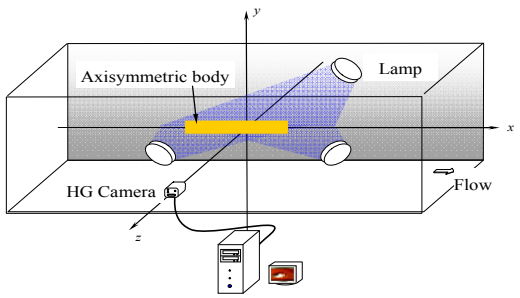

(b)

Fig. 1. The sketch of cavitation tunnel and schematic of an axisymmetric body and the test section.

to control the pressure in the tunnel. Between the test section and the tank, a corner vane and a straightening vane are used to reduce the turbulence level of the flow in the test section [6].

The schematic of an axisymmetric body with a blunt headform and the test section are shown in Fig. 1(b). The axisymmetric body's length L is 0.12 m and its diameter D is 0.02 m, respectively. The test section is 0.7 m in length, 0.19 m in height, and 0.07 m in width. The flow field near the axisymmetric body is well lighted by three high-energy lamps, and the cavitation phenomena is documented by a high-speed digital camera (HG-LE, by Redlake), up to a rate of 10^5 frames per second (fps). In order to maintain the desired spatial resolution, a much lower recording speed is adopted. Specifically, depending on the focus of the investigation, 5000 fps is used in this study. The cavitation phenomena are documented from the side view, and then stored in a computer for post processing.

Cavitation number and Reynolds number are defined as below:

$$\sigma = (p_\infty - p_v)/0.5\rho U_\infty^2, \quad Re = U_\infty d_n / \nu$$

where p_∞ is the reference static pressure, p_v is the saturated vapor pressure of water, ρ is the water density, U_∞ is the reference velocity, ν is the dynamic viscosity of water, and D is the diameter of axisymmetric body. In this study, the

reference velocity U_∞ is fixed at 8.5 m/s, the Reynolds number equals to 1.76×10^5. The reference static pressure can be controlled by vacuum pump to adjust cavitation number. In the present study, $\sigma=0.7$ and $\sigma=0.6$ are chosen for investigation. The uncertainty of the electromagnetic flowmeter is 0.5 %, and the uncertainty of the pressure transducer is 0.25 %. The cavitation number, where p_∞ is the tunnel pressure can be controlled to within a 5 % uncertainty.

For the numerical calculation, the commercial software ANSYS-CFX [25] is applied to simulate the unsteady cavitating flows. The homogeneous equilibrium flow theory is used here and the continuity and momentum equations for the mixture flow in the Cartesian co-ordinates are as below:

$$\frac{\partial\rho_m}{\partial t}+\frac{\partial(\rho_m u_j)}{\partial x_j}=0 \tag{1}$$

$$\frac{\partial(\rho_m u_i)}{\partial t}+\frac{\partial(\rho_m u_i u_j)}{\partial x_j}=-\frac{\partial p}{\partial x_i}+\frac{\partial}{\partial x_j}[(\mu+\mu_t)\left(\frac{\partial u_i}{\partial x_j}+\frac{\partial u_j}{\partial x_i}-\frac{2}{3}\frac{\partial u_i}{\partial x_j}\delta_{ij}\right)] \tag{2}$$

where u is the velocity, ρ_{m} is the mixture density, p is the pressure, μ and μ_t are the laminar and turbulent viscosity, and the subscripts i, j are the directions of the axes.

Cavitation process is governed by the transport equation for the liquid volume fraction given in Eq. (3) which ignores the thermal energy and nonequilibrium-phase change effects. In the present work, the source term $\dot{m}^+$ and $\dot{m}^-$ represent the condensation and evaporation rates which are modeled by Zwart cavitation model [26].

$$\frac{\partial\alpha_l}{\partial t}+\frac{\partial(\alpha_l u_j)}{\partial x_j}=\dot{m}^++\dot{m}^- \tag{3}$$

$$m^-=F_e\frac{3\alpha_{nuc}(1-\alpha_v)\rho_v}{R_B}\sqrt{\frac{2}{3}\frac{|p_v-p|}{\rho_l}} \tag{4}$$

$$m^+=F_c\frac{3\alpha_v\rho_v}{R_B}\sqrt{\frac{2}{3}\frac{|p_v-p|}{\rho_l}} \tag{5}$$

where F_e and F_c are empirical coefficients for vaporization and condensation processes, α_{nuc} is the volume fraction of the nucleation sites, and R_B is the radius of nucleation sites. These parameter values are respectively set to $\alpha_{nuc}=5e-4$, $R_B=1\ \mu$m, $F_e=50$ and $F_c=0.01$.

As to the turbulent model, based on the original PANS model proposed by Girimaji et al. [13], in this work a modified PANS model [19] is used in the ANSYS-CFX code. The following govern equation presents the modification and it shows that the ratio of the unresolved-to-total kinetic energy f_k is not a constant but can vary with the flow density. Fig. 2 demonstrates that f_k is decreasing with cavitation developing.

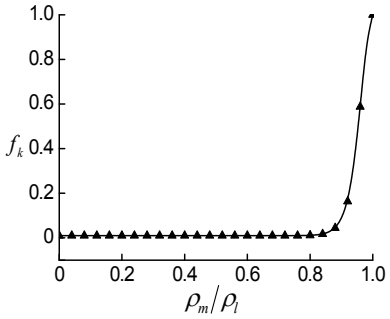

Fig. 2. The values of control variable f_k versus the density ratios.

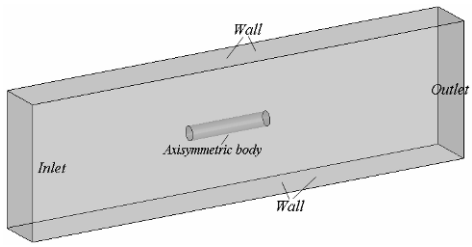

(a)

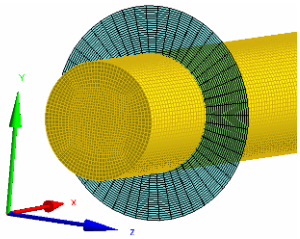

(b)

Fig. 3. Computational domain and the mesh around the body surface.

$$f_k=\tanh(\operatorname{atanh}C_2\times(\rho_m/\rho_l)^{C_1})+1-C_2 \quad (C_1\geq1, 0<C_2<1). \tag{6}$$

Here, $C_1=34.05$, $C_2=0.99$, ρ_m is the mixture density, and ρ_l is the water density.

Fig. 3(a) shows the computational domain which is consistent with the experimental setup. The boundary conditions imposed velocity at inlet, static pressure at outlet, no-slip wall on the axisymmetric body and the free-slip wall on the four side surfaces of the domain. It should be noted that the flow Reynold number and cavitation number are adapted depending on the experimental data. Fig. 3(b) gives the sketch of mesh around the axisymmetric body. The fine resolution mesh with about 1.5 million nodes for the fluid domain is selected here, and the comment about the validation of mesh and the present numerical method can be found in Ref. [9].

3. Results and discussions

Figs. 4 and 5 respectively show the time-evolution of predicted and experimental cavity morphology at $\sigma=0.7$ and $\sigma=0.6$. For the both cases, the unsteady cavitating flow

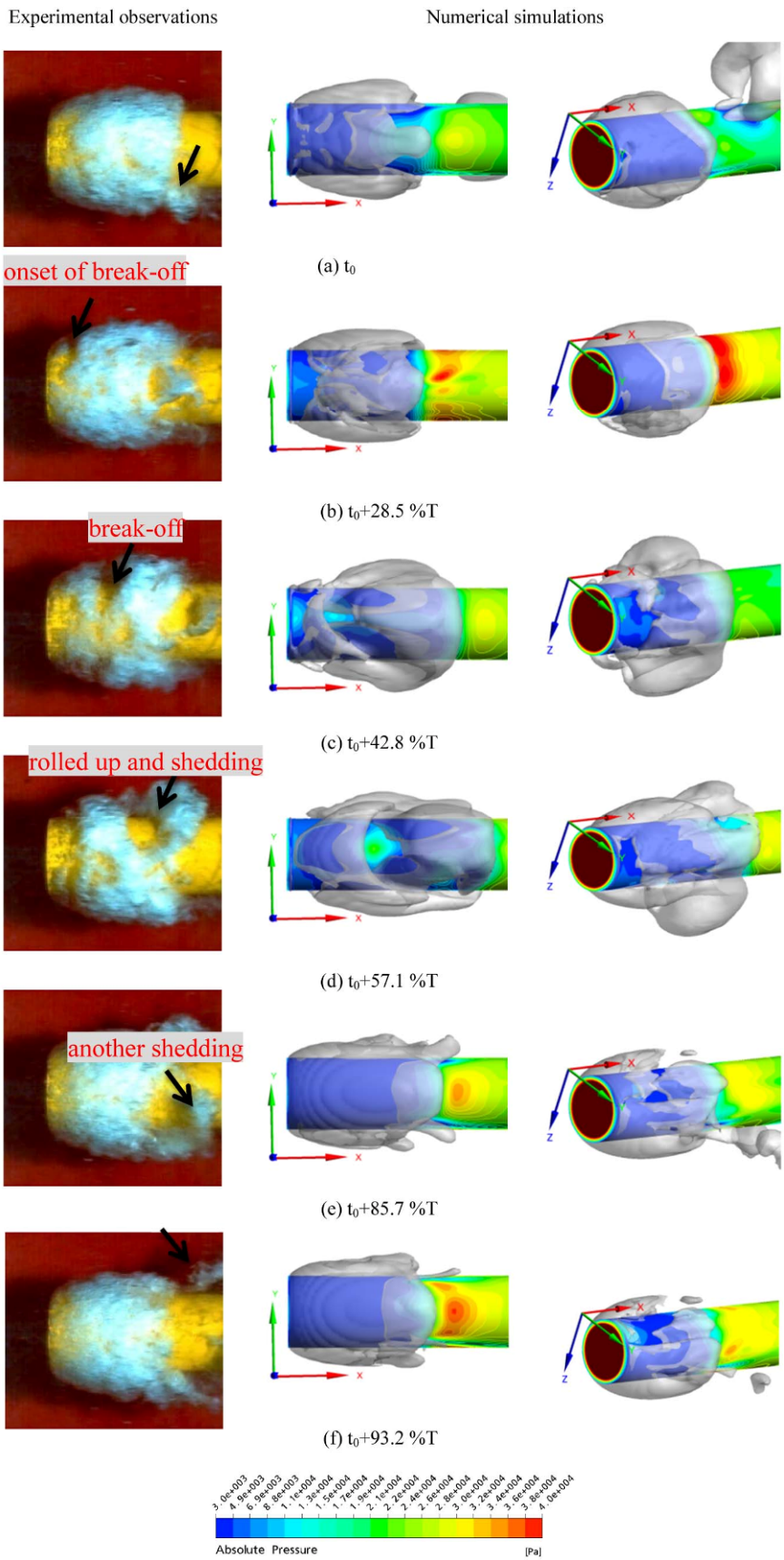

Fig. 4. Time-evolution of cavity shedding in one typical cycle (σ = 0.7).

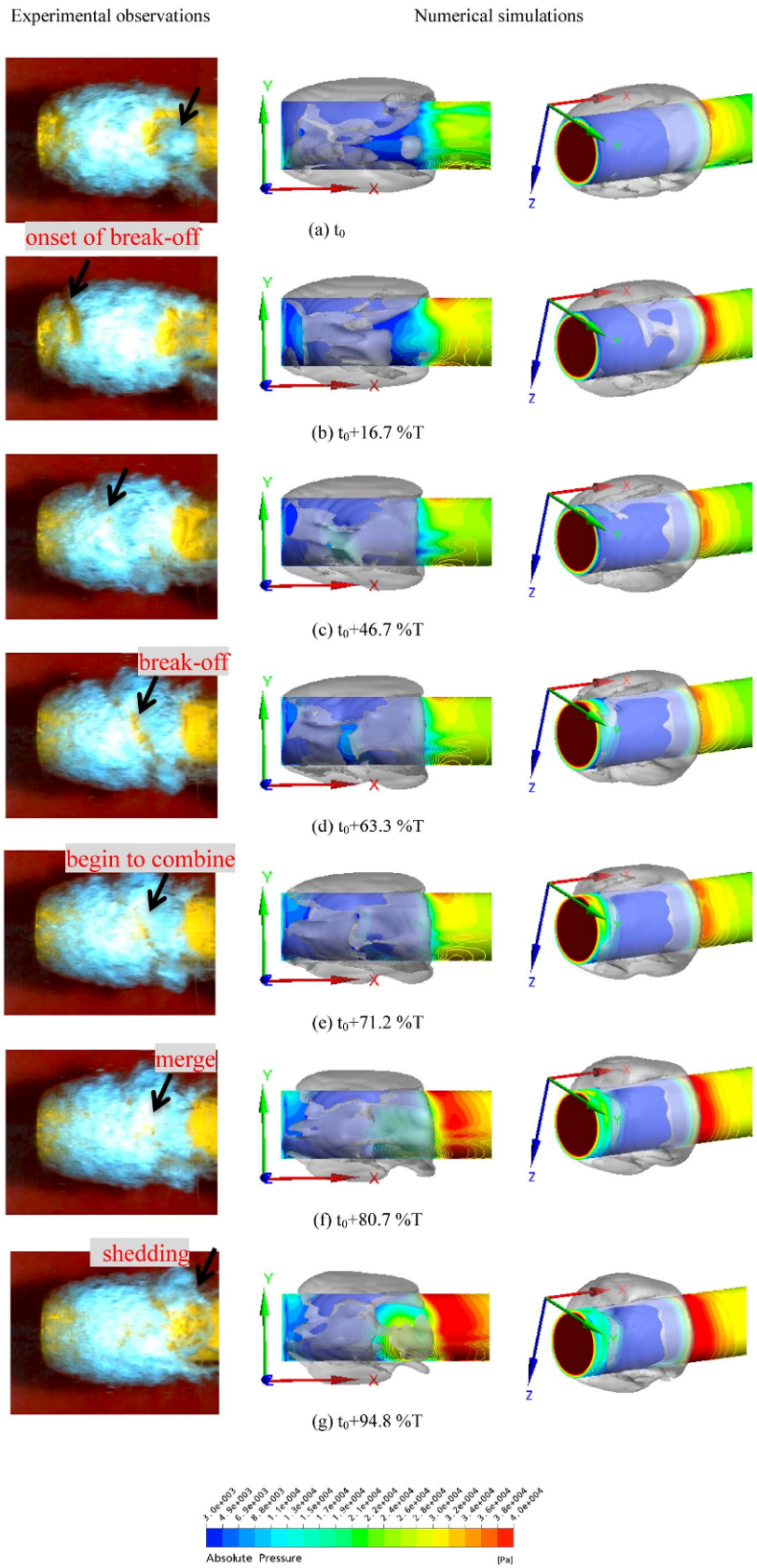

Fig. 5. Time-evolution of cavity shedding in one typical cycle (σ = 0.6).

structures evolve periodically, and the predicted periods of cavity evolutions are longer than that from the experiment. Thus, in order to make better comparisons of simulated results and experimental data, the transient snapshots of cavity are listed in sequence of their own cycles marked as T in the present work. The numerical cavity shape is illustrated by the iso-surface of water vapor volume fraction of 0.2. Meanwhile, the surface of axisymmetric body is colored by absolute pressure. The average values of cavity maximum length from experiment are about 2.28 D and 1.76 D for $\sigma = 0.6$ and $\sigma = 0.7$, respectively which are both slightly smaller than the present computational results of 2.3 D at $\sigma = 0.6$ and 1.8 D at $\sigma = 0.7$. However, the predicted cavity shedding process of $\sigma = 0.7$ and $\sigma = 0.6$ both agree reasonably well with experimental observations. As in the experiment, the modeled cavity at the two cavitation indices undergoes a similar process which can be simply described as the previous attached cavity followed by irregular break-off, U-type shedding and another attached cavity growing again. Furthermore, both numerical and experimental results show that the vapor distribution around the body is highly asymmetric and presents three-dimensional characteristics, which is possibly relevant to the motion of reentrant flow driven by the high pressure region downstream of the cavity. The similar comments are also proposed by Lindau et al. [27]. To make comparisons of Figs. 4 and 5, it is found that there are substantial differences in the details of cavity shedding process between $\sigma = 0.7$ and $\sigma = 0.6$. Focused on Figs. 4(c) and (d), a large bulk of aft end cavity is rolled up and sheds downstream, which leads to the evolution of cavity to show violent and turbulent. While in Figs. 5(c)-(f), it can be seen that after the attached cavity breaking off, the shedding part trends to combine with the main bulk of cavity again, and after a while it just shed in the form of smaller scale cavity.

The dynamic forces of the axisymmetric body at $\sigma = 0.7$ and $\sigma = 0.6$ are also numerically investigated. Fig. 6 contains the time-evolution fluctuations of axial force coefficients as well as the comparison of fluctuant variances at the two cavitation numbers. In Fig. 6(a), the highlighted points on the curves separately corresponds to the cavity images listed in Figs. 4 and 5. Here, the parameter T_{ref} is defined as $T_{ref} = D / U_{\infty}$. It can be found that the axial force always increases when the large bulk of cavity breaks off or rolls up. Compared with that of $\sigma = 0.6$, the fluctuation amplitude of the axial force at $\sigma = 0.7$ is larger and also the time-averaged axial force is at higher level. Besides, from Fig. 6(b), the variance of axial force at $\sigma = 0.7$ is about three times as large as that of $\sigma = 0.6$, which demonstrates that there are more fluctuations and instabilities during the whole time-evolution process of unsteady cavity at $\sigma = 0.7$.

Lagrangian tracers are utilized in this study to further investigate the cavity shedding process at $\sigma = 0.7$ and $\sigma = 0.6$. The magnitude of the integration time T_{LE} used to compute the FTLE is 0.9 T. Figs. 7 and 8 present the vapor volume fraction contours and the particle tracers at three typical instants. The

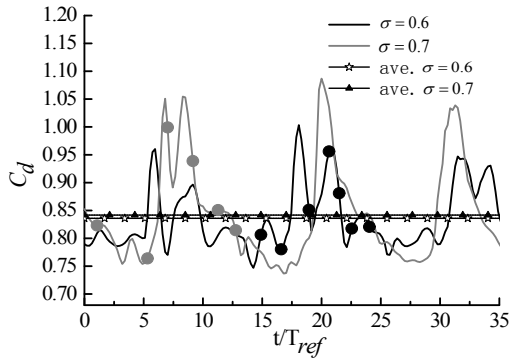

(a) Time-evolution of axial force coefficients

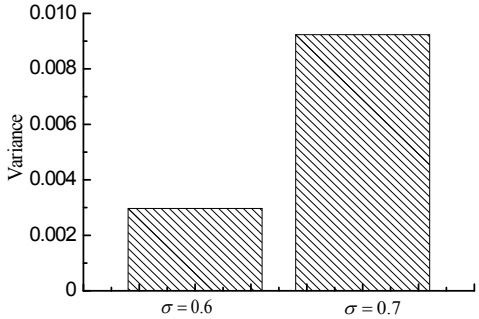

(b) Variance of axial force coefficients

Fig. 6. The predicted fluctuations of axial force coefficient at different cavitation numbers.

four groups of particle tracers marked by "A", "B", "C" and "D" are initially seeded at the positions of x = 0.01 m, x = 0.02 m, x = 0.03 m and x = 0.04 m, respectively in the flow field. The particle tracers will move with the development of cavitating flow, which can illustrate the time-evolution of cavitating flow structures. As shown in Fig. 7, the first group of tracers named "A" is located upstream of the position where the attached cavity breaks off, however, the last three groups of tracers named "B", "C" and "D" are located in the downstream where detached cavities exist. At t = t_0+57.1 %T, as illustrated by the tracers in group "A", re-entrant flow exists accompanying the growth of attached cavity. The tracers in group "B", "C" and "D" also show that re-entrant flow exist in the downstream, and most tracers in group of "C" and "D" move away from the cylinder surface, which elucidates the rolling up of detached cavity. After t = t_0+62.2 %T, tracers in group of "A" move downstream along the attached cavity surface. Tracers in group "B" and part of the tracers in group "C" move upstream toward the head of cylinder. Tracers in group "D" and part of the tracers in group "C" move downstream and away from the cylinder surface due to the behavior of rolling up and movement of the detached cavity.

Similarly, the time evolution of lagrangian tracers in cavitating flow at $\sigma = 0.6$ is presented in Fig. 8. There are four groups of tracers which are named "A", "B", "C" and "D", respectively. In the period after t = t_0+63.3 %T, tracers in group "A" move upstream, which also illustrates the existence

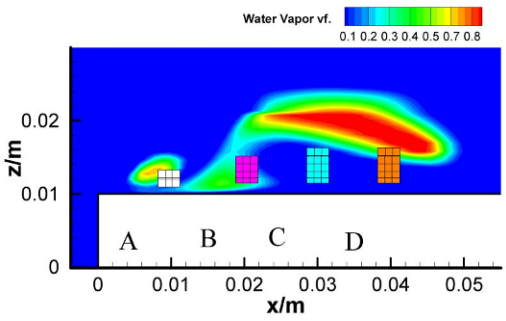

(a) t_0+42.8 %T

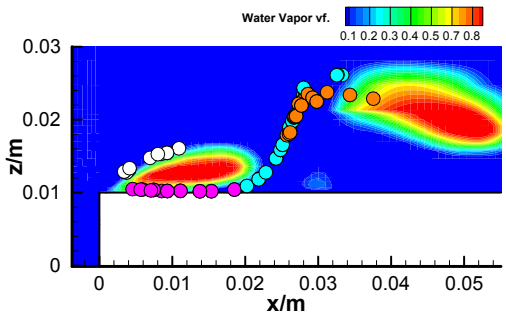

(b) t_0+57.1 %T

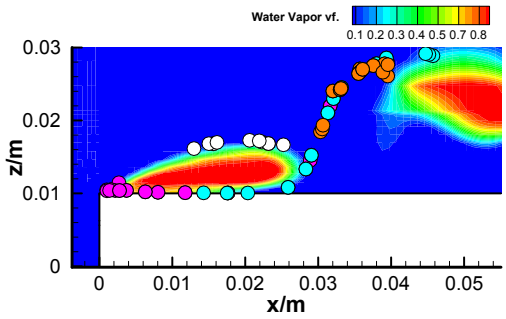

(c) t_0+62.2 %T

Fig. 7. The contours of water vapor fraction and the distributions of Lagrangian tracers ($\sigma = 0.7$).

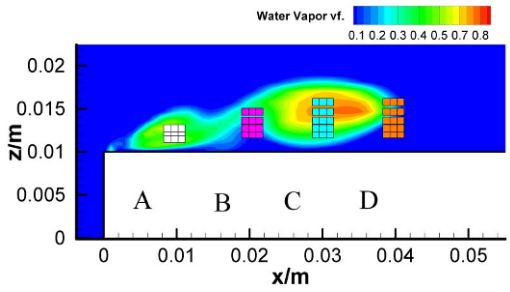

(a) t_0+46.7 %T

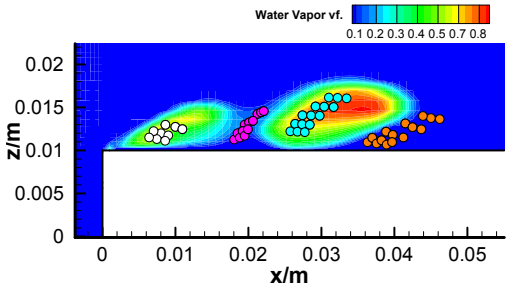

(b) t_0+63.3 %T

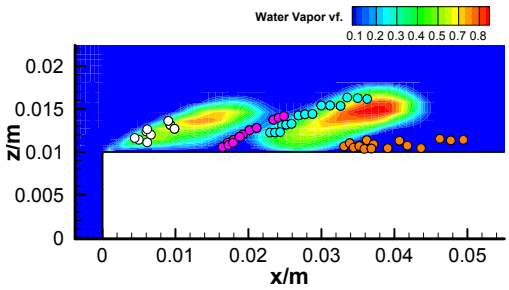

(c) t_0+71.2 %T

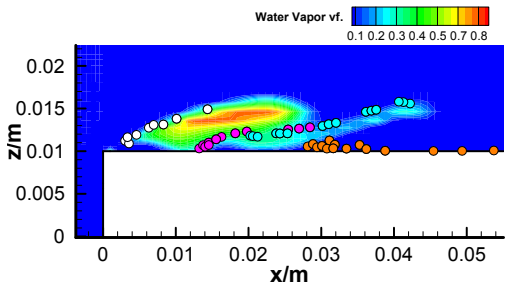

(d) t_0+94.8 %T

Fig. 8. The contours of water vapor fraction and distributions of Lagrangian tracers ($\sigma = 0.6$).

of re-entrant flow. Tracers in group "B", "C" and "D" move upstream and downstream at the same time, consequently, the cavity in the region near group "C" is elongated. After t = t_0+71.2 %T, the tracers in group "B" and "C" move upstream and downstream further, and the attached cavity and detached cavity begin to merge. Finally, tracers in group "B" and "C" are mixed together, and accordingly the attached cavity merge into the detached part.

To evaluate the flow field characteristics, Figs. 9 and 10 give respectively the instantaneous streamlines, the contours of FTLE, and the Lagragian tracer trajectory at $\sigma = 0.7$ and $\sigma = 0.6$. The Lagragian tracer trajectory can demonstrate the movement of local fluid element in the period of integration time. Here, each figure presents eight tracer trajectories to help to describe the flow structures. The initial locations of eight particles for the two cases are respectively listed in Tables 1 and 2 where x is the axial distance and y is the distance from the body wall in the radial direction. Compared with the streamlines, it is found that the ridges of FTLE field almost match the outer edges of vortex structures and divide the field into different flow regions. Also, the particles always move along the ridge instead of across it. From Fig. 9, it is found that a large scale of vortex is located at the forehead of axisymmetric body at t_0+28.5 %T when the whole cavity is attached as shown in Fig. 4. Accordingly, most of the particles initially located within the vortex move upstream. Then at t_0+42.8 %T the cavity breaks off into two parts due to the re-

Table 1. The initial locations of Lagrangian tracers ($\sigma = 0.7$).

Point No.	0	1	2	3	4	5	6	7
x/(m)	0	0.01	0.02	0.03	0.035	0.04	0.05	0.01
y/(m)	0.001	0.004	0.004	0.004	0.002	0.004	0.004	0.001

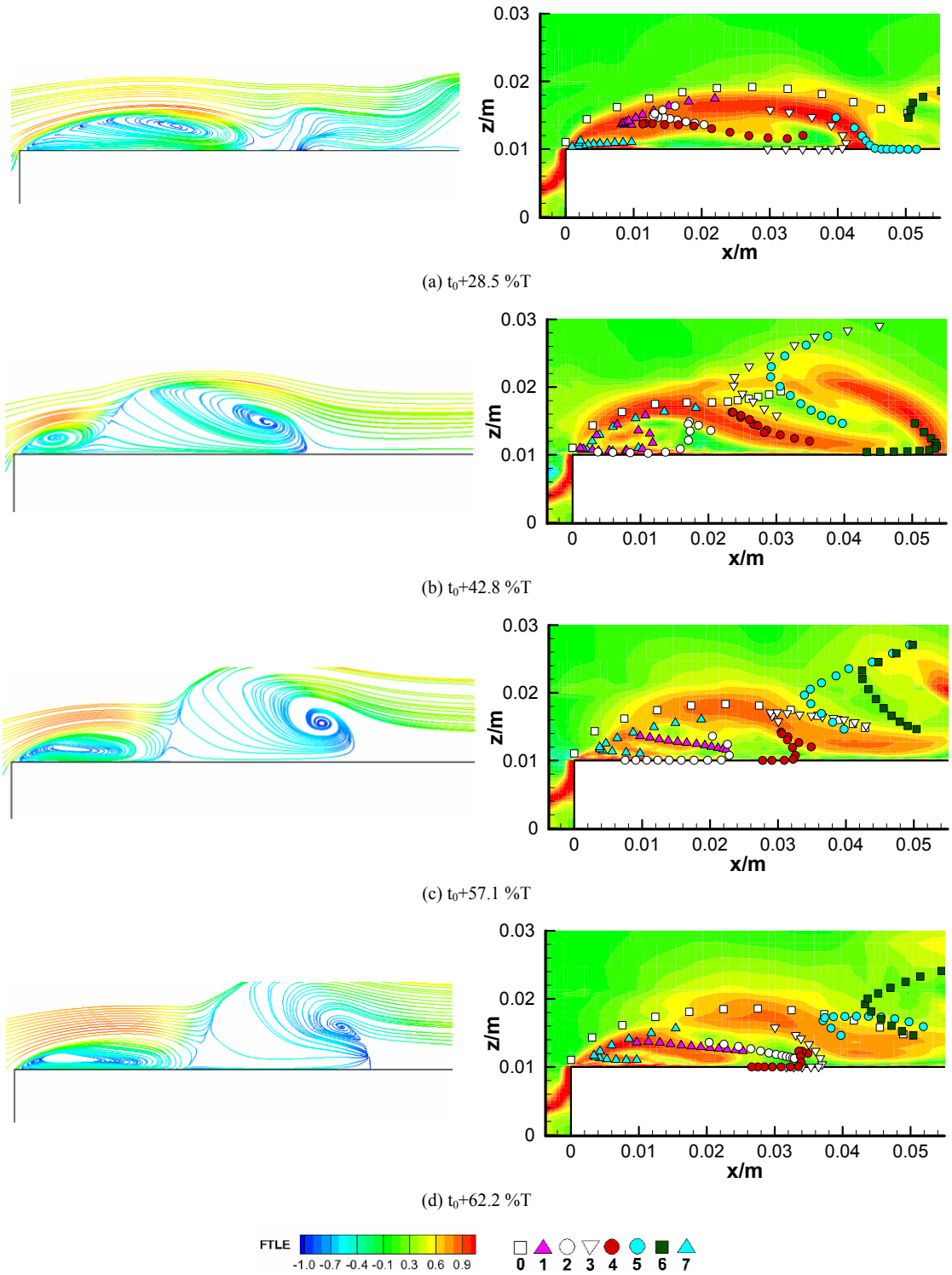

(a) t_0+28.5 %T

(b) t_0+42.8 %T

(c) t_0+57.1 %T

(d) t_0+62.2 %T

Fig. 9. The streamlines, FTLE contours and distributions of Lagrangian tracers ($\sigma = 0.7$).

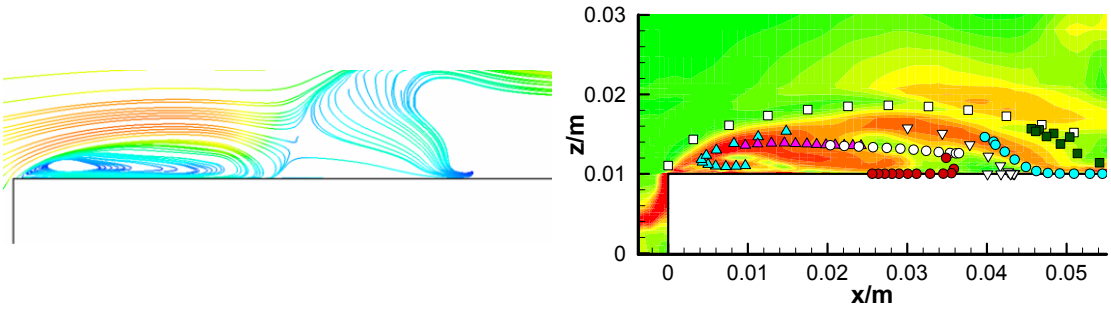

(e) t_0+69.6 %T

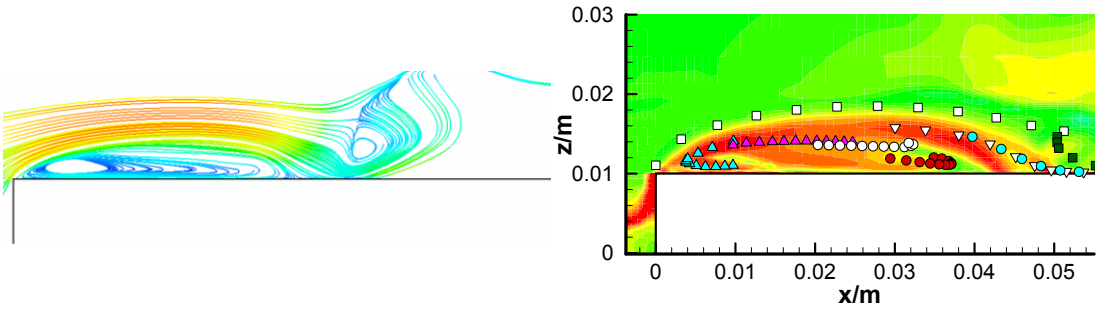

(f) t_0+75.2 %T

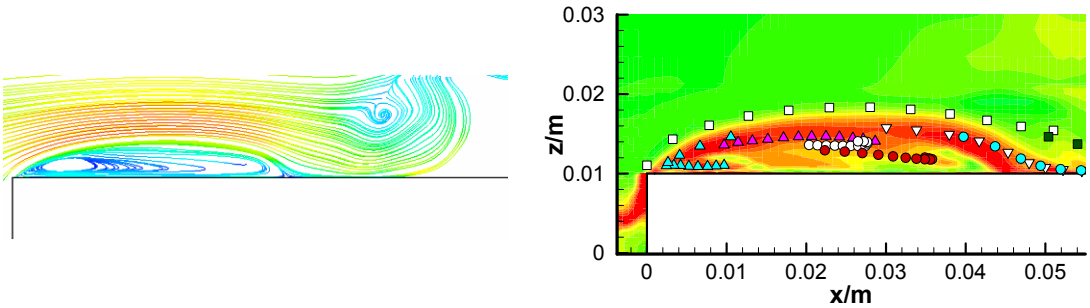

(g) t_0+79.8 %T

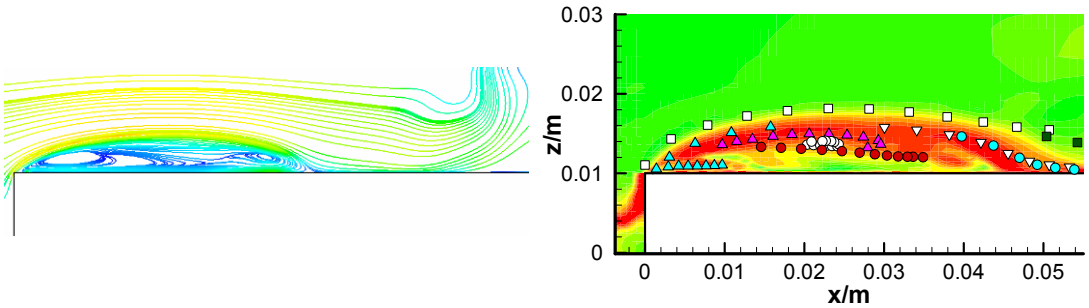

(h) t_0+85.7 %T

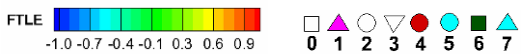

Fig. 9. (Continued).

entrant flow, and in Fig. 9(b) the flow field presents two vortex structures with the same rotation direction but different scales. Moreover, the trajectories of particles 3 and 5 indicate that the downstream vortex of larger scale gradually moves away from the body surface, which is consistent with the cavity rolling-up process. By contrast, in Fig. 10, during the process of cavity breaks off at $\sigma = 0.6$ there is no large scale of cavity rolling up, therefore the two vortex structures always adhere to each other and neither breaks away from the body surface. In the next period, the upstream vortex spreads to a large one again which means a new evolution cycle beginning, while the downstream one gradually shrinks to disappear finally.

Table 2. The initial locations of Lagrangian tracers ($\sigma = 0.6$).

Point No.	0	1	2	3	4	5	6	7
x/(m)	0	0.01	0.015	0.025	0.03	0.035	0.035	0.01
y/(m)	0.001	0.004	0.004	0.004	0.004	0.004	0.001	0.001

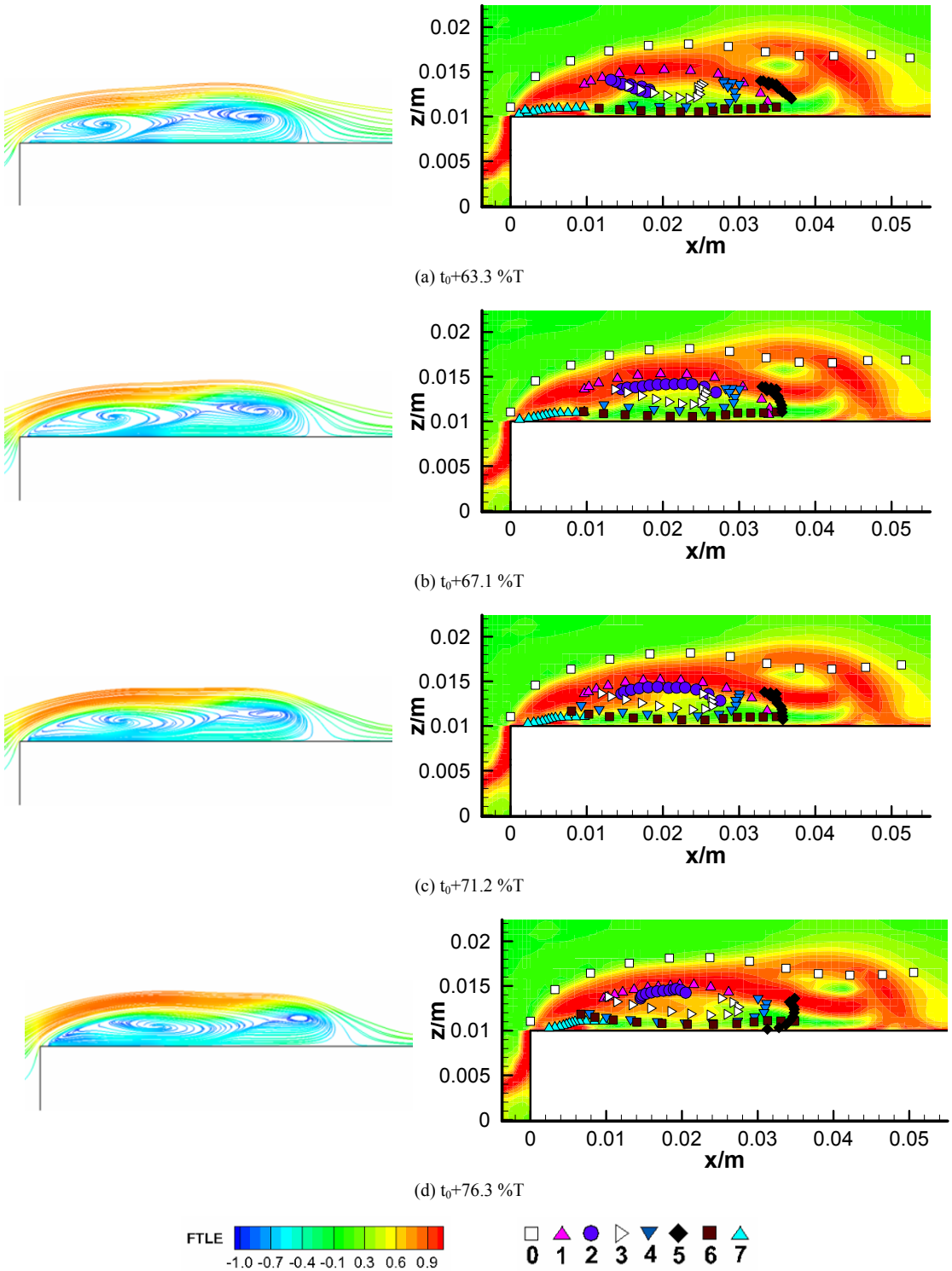

Fig. 10. The streamlines, FTLE contours and distributions of Lagrangian tracers ($\sigma = 0.6$).

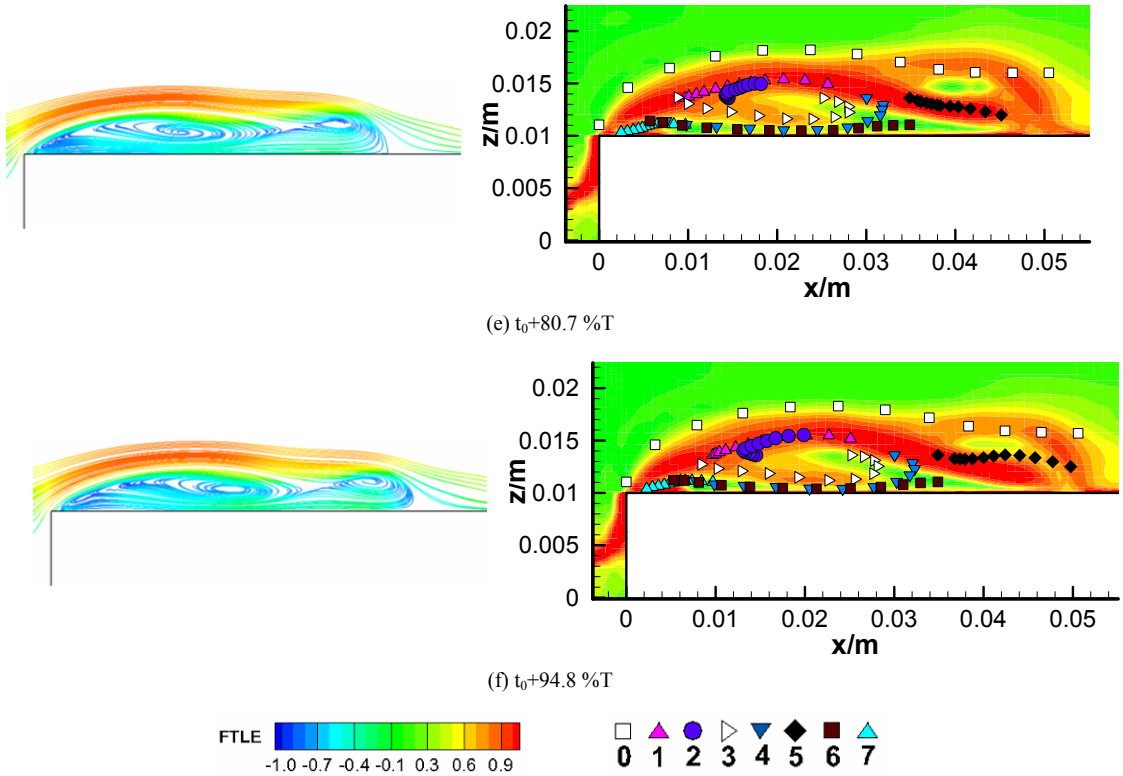

Fig. 10. (Continued).

4. Conclusions

In this research, unsteady cavitating flows around an axisymmetric blunt body at two different cavitation numbers have been investigated experimentally and numerically. The main attention is focused on the cavity shedding dynamics. The LCS and particle trajectory methods are applied to demonstrate the mechanism of shedding behaviors. Here some findings are summarized:

(1) The numerical cavitation evolutions are in good agreements with the experimental results for the both flow conditions of $\sigma = 0.7$ and $\sigma = 0.6$. The similar process of cavity evolutions is found for the two cases including irregular break-off of attached cavity, shedding of the detached part and growing again of the remaining part. However, there are also some distinct characteristics during the shedding process. When $\sigma = 0.7$, the shedding cavity can roll up and detach away from the body, while at $\sigma = 0.6$ the break-off cavity can reconstruct through the conjunction behavior. This is probably responsible for the different fluctuations of axial force of the blunt body. In this study it is found that the variance of axial force at $\sigma = 0.7$ is almost three times as large as that of $\sigma = 0.6$.

(2) The LCS and particle trajectory methods can well illustrate the flow structures during the shedding process. The LCS distributions vary with the time-evolution of vortex structures that exactly vary with the cavity shedding behaviors. When $\sigma = 0.7$, the downstream detached vortex moves away from body, while at $\sigma = 0.6$ the upstream and downstream vortex structures can connect together. Moreover, the particle trajectories can illustrate the behaviors of local flow to explain the mechanism of the two shedding modalities.

Conflict of interest

There is no conflict of interest.

Acknowledgements

This work is supported by the Natural Science Foundation of Jiangsu Province (Grant No.BK20150764), the Fundamental Research Funds for the Central Universities (Grant No.30916011333) and the National Natural Science Foundation of China (Grant No.51606097).

References

[1] R. T. Knapp, J. W. Daily and F. G. Hammitt, *Cavitation*, McGraw-Hill, New York, USA (1970).

[2] C. E. Brennen, *Cavitation and bubble dynamics*, Oxford University Press, New York, USA (1995).

[3] G. Y. Wang et al., Dynamics of attached turbulent cavitating flows, *Progress in Aerospace Sciences*, 37 (6) (2001) 551-581.

[4] A. Kubota et al., Unsteady structure measurement of cloud cavitation on a Foil section using conditional sampling tech-

nique, *Journal of Fluid Engineering*, 111 (2) (1989) 204-210.
[5] J. B. Leroux, J. A. Astolfi and Y. Billard, An experimental study of unsteady partial cavitation, *Journal of Fluid Engineering*, 126 (2004) 94-101.
[6] B. Huang et al., Combined experimental and computational investigation of unsteady structure of sheet/cloud cavitation, *Journal of Fluids Engineering*, 135 (2013) 071301-1-071301-16.
[7] H. Rouse and J. S. McNown, Cavitation and pressure distribution: head forms at zero angle of yaw, *Proactive Maintenance for Mechanical Systems* (1948) 169-191.
[8] H. Liu and Y. S. He, Frequency characteristics of unsteady cavitating flows around axisymmetric headforms, *Proceedings of the Eighth International Symposium on Cavitation*, Singapore, August 13-16 (2012).
[9] C. L. Hu et al., Three-dimensional unsteady cavitating flows around an axisymmetric body with a blunt headform, *Journal of Mechanical Science and Technology*, 29 (2015) 1093-1101.
[10] O. Coutier-Delgosha, R. Fortes-Patella and J. L. Reboud, Evaluation of the turbulence model influence on the numerical simulations of unsteady cavitation, *Journal of Fluids Engineering*, 125 (1) (2001) 38-45.
[11] J. Wu, S. T. Johansen and W. Shyy, Filter-based unsteady RANS computations for single-phase and cavitating flows, *ASME 2004 Heat Transfer/Fluids Engineering Summer Conference,* American Society of Mechanical Engineers, 3 (2004) 469-477.
[12] B. E. Launder and D. B. Spalding, The numerical computation of turbulent flows, *Computer Methods in Applied Mechanics & Engineering*, 3 (1974) 269-289.
[13] S. S. Girimaji and K. S. Abdol-Hamid, Partially averaged navier-stokes model for turbulence: Implementation and validation, *AIAA Paper*, 502 (2005) 2005.
[14] B. Ji, X. W. Luo, R. E. A. Arndt, X. Peng and Y. Wu, Large eddy simulation and theoretical investigations of the transient cavitating vortical flow structure around a NACA66 hydrofoil, *International Journal of Multiphase Flow*, 68 (2015) 121-134.
[15] X. Yu et al., Study of characteristics of cloud cavity around axisymmetric projectile by large eddy simulation, *Journal of Fluids Engineering*, 136 (2014) 051303.
[16] J. Yang, L. J. Zhou and Z. W. Wang, Numerical simulation of three-dimensional cavitation around a hydrofoil, *Journal of Fluids Engineering*, 133 (2011) 081301.
[17] B. Ji, X. W. Luo, Y. L. Wu and K. Miyagawa, Numerical investigation of three-dimensional cavitation evolution and excited pressure fluctuations around a twisted hydrofoil, *Journal of Mechanical Science and Technology*, 28 (2014) 2659-2668.
[18] Y. Chen, C. J. Lu, X. Chen and J. Y. Cao, Numerical investigation on the cavitation collapse regime around the submerged vehicles navigating with deceleration, *European Journal of Mechanics / B Fluids*, 49 (2015) 153-170.
[19] C. L. Hu, G. Y. Wang, G. H. Chen and B. Huang, A modified pans model for computations of unsteady turbulence cavitating flows, *Science China-Physics Mechanics & Astronomy*, 57 (10) (2014) 1967-1976.
[20] G. Haller and G. Yuan, Lagrangian coherent structures and mixing in two-dimensional turbulence, *Physica D*, 147 (2000) 352-370.
[21] S. C. Shadden, F. Lekien and J. E. Marsden, Definition and properties of Lagrangian coherent structures from finite-time Lyapunov exponents in two-dimensional aperiodic flows, *Physica D*, 212 (2005) 271-304.
[22] M. A. Green, C. W. Rowley and G. Haller, Detection of Lagrangian coherent structures in three-dimensional turbulence, *Journal of Fluid Mechanics*, 572 (2007) 111-120.
[23] W. Tang, M. Mathur, G. Haller, D. C. Hahn and F. H. Ruggiero, Lagrangian coherent structures near a subtropical jet stream, *Journal of the Atmospheric Sciences*, 67 (2010) 2307-2319.
[24] Y. Zhao, G. Y. Wang, B. Huang and Q. Wu, Lagrangian investigations of vortex dynamics in time-dependent cloud cavitating flows, *International Journal of Heat and Mass Transfer,* 93 (2016) 167-174.
[25] *ANSYS CFX Tutorials*, ANSYS Inc.
[26] P. J. Zwart, A. G. Gerber and T. Belamri, A two-phase flow model for predicting cavitation dynamics, *Proc. of the Fifth International Conference on Multiphase Flow*, Yokohama, Japan (2004) 152.
[27] J. W. Lindau, R. F. Kunz, D. A. Boger, D. R. Stinebring and H. J. Gibeling, High Reynolds number, unsteady, multiphase CFD modeling of cavitating flows, *Journal of Fluid Engineering*, 124 (2002) 607-616.

Changli Hu obtained her Ph.D. in School of Mechanical Engineering from Beijing Institute of Technology of China in 2015. She mainly works on the experimental and numerical studies of cavitating flows, and the optimal method of the underwater body.